

See discussions, stats, and author profiles for this publication at: <https://www.researchgate.net/publication/258250484>

Homo- and Hetero- p-n Junctions Formed on Graphene Steps

ARTICLE in ACS APPLIED MATERIALS & INTERFACES · NOVEMBER 2013

Impact Factor: 6.72 · DOI: 10.1021/am402808p · Source: PubMed

CITATIONS

5

READS

69

4 AUTHORS, INCLUDING:



Weiguang Xie

Jinan University (Guangzhou, China)

54 PUBLICATIONS 342 CITATIONS

SEE PROFILE



Jian Chen

Sun Yat-Sen University

120 PUBLICATIONS 2,690 CITATIONS

SEE PROFILE

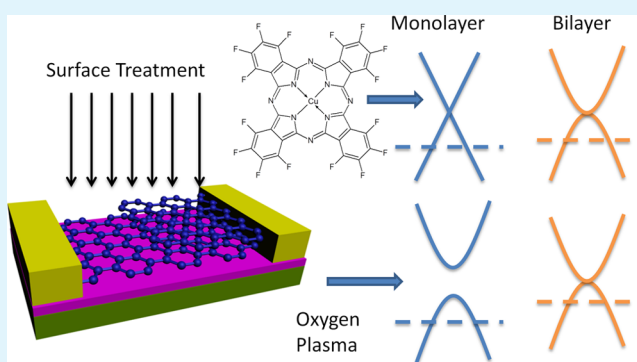
Homo- and Hetero- p–n Junctions Formed on Graphene Steps

Xiaomu Wang,[†] Weiguang Xie,[‡] Jian Chen,[§] and Jian-Bin Xu^{*,†}[†]Department of Electronic Engineering and Materials Science and Research Technology Center, The Chinese University of Hong Kong, Shatin, N. T., Hong Kong SAR, China[‡]Siyuan Laboratory, Department of Physics, Jinan University, Guangzhou, Guangdong, P. R. China[§]Instrumental Analysis & Research Center, Sun Yat-sen University, Guangzhou 510275, P. R. China

Supporting Information

ABSTRACT: p–n junction is a fundamental building block in modern electronic circuits. We report graphene p–n junctions formed by a one-step thickness-dependent surface treatment of mono-/bilayer graphene steps. The junction electronic properties are systematically studied by means of Kelvin probe force microscopy (KPFM) and transport measurements. Because of the dissimilar modifications to graphene electronic properties, the junctions behave distinctly, i.e., two-component resistance-like for organic charge transfer doping and Shottky-junction-like for covalent doping. By exploring the spatially potential distribution, we clarify the potential profiles as well as the transport attributes across the graphene p–n junction interface under lateral bias and electrical gating. Our results not only unveil the detailed properties of graphene p–n junction interface, but also gain an insight into its practical applications in nanoelectronics.

KEYWORDS: graphene, p–n junction, electronic properties, KPFM



INTRODUCTION

Graphene, a new allotrope of carbon, is an appealing material for post-silicon nanoelectronics. With its superior electronic properties and great potential, graphene is expected to be a good candidate for next generation semiconductor technology.^{1–3} Of both scientific and technical importance are doped graphene p–n junctions, which also serve two-different merits simultaneously. On the one hand, graphene p–n junction offers numerous intriguing transport properties and provides crucial conceptual justifications such as quantum Hall effect,⁴ Klein tunneling,⁵ nonlinear screening,⁶ and perfect lensing.⁷ On the other hand, p–n junction is a fundamental building block in modern semiconductor industry and of technological interest for electronic devices. However, because of the zero-bandgap properties, a potential barrier is usually absent in graphene p–n junctions, which detrimentally impacts the junction application (e.g., absence of rectification effect). The ability to apply graphene p–n junctions as practical electronic devices still remains open to be elucidated.

A large number of asymmetric doping approaches have been reported to generate complementary doping levels in a single graphene flake. For instances, double gates,^{8,9} spatial selective doping,^{10–12} complementary chemical doping,^{13–16} and electrical stress^{17–19} have been demonstrated to form graphene p–n junctions. Recently, we have illustrated an alternative approach that does not require multiple doping processes or additional lithographic structures.²⁰ By a one-step thickness-

dependent surface treatment of graphene samples with different layer numbers at terraces, the workfunctions jump across a specific layer boundary (a step), which renders the band bending and p–n junction. This surface doping strategy provides several advantages. First, the treatment process is scalable and resist-free which are suitable for nano-fabrication process. Second, the uncovered graphene top surface makes it possible to apply surface characterization tools such as scanning probe microscopy or Raman spectroscopy to study the potential profiles. Third, the sharp boundaries between different layers naturally provide well-defined abrupt interfaces.

In this letter, we fabricate graphene p–n junctions by treating graphene steps, with either surface charge transfer or covalent functionalization. We systematically study the attributes across the graphene p–n junction interface by utilizing Kelvin probe force microscopy (KPFM) and transport measurements. We find that the junction behavior changes distinctly for different surface treatments. Although both junctions manifest the nonuniform electronic modification by occurrence of a second charge neutrality point (CNP) in the transfer characteristics; organic charge transfer doping slightly alters the output characteristics besides appreciable negative differential resistance (NDR) effects, whereas the covalent doping approach

Received: July 15, 2013

Accepted: November 1, 2013

Published: November 1, 2013



gives rise to obvious rectifier effects. The in situ KPFM which enables the simultaneously electrical and surface potential measurements shows that the different electronic structures and screening properties of functionalized graphene induced by different surface treatments result in the adjusted band profiles in the respective domains (segments) around the junction interfaces and the changed output characteristics. Our results not only exemplify two typical kinds of graphene p–n junctions, namely, homo- and hetero- junctions; but also reveal the spatial potential distribution and field-effect response along the junction interface. In addition, we provide an evidence of operational graphene-based negative-differential-resistance (NDR) device and rectifier. Our findings gain deep insights into graphene p–n junctions and pave the way for their practical applications.

■ EXPERIMENTAL SECTION

Our graphene p–n junctions are formed by treating a graphene step across a monolayer region and a bilayer region, as shown in Figure 1a.

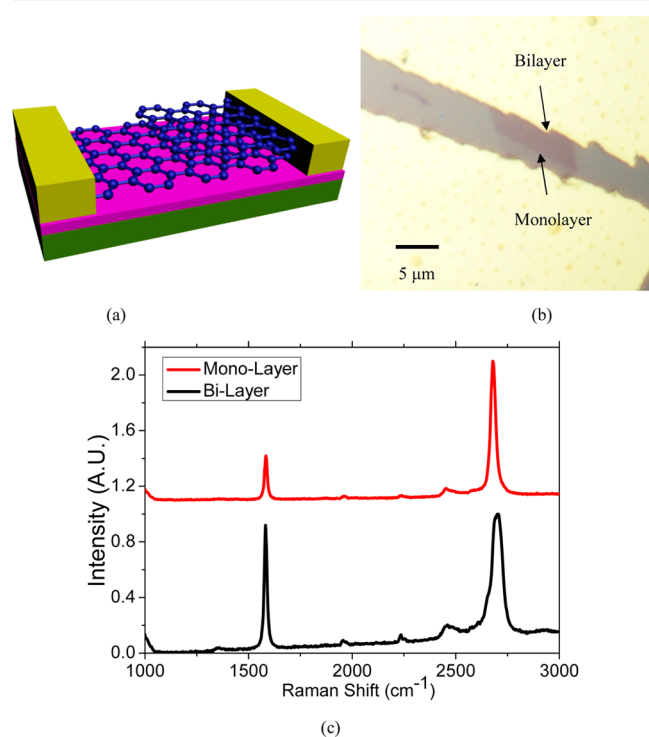


Figure 1. (a) Schematic of mono-/bilayer graphene step devices. (b) Typical graphene step device. The layer number connected to each electrode is labeled. (c) Raman spectra of the as-prepared graphene step in b. The small D peak observed here may arise from the edge effect.

It is worth noting that although the band structures are not exactly equal in the two regions, the electronic behaviors are quite similar for mono- and bilayer graphene, and the step can be regarded as a single graphene device, which will be verified by the uniform transport nature of as-prepared graphene step as to be demonstrated below. Graphene samples are prepared by mechanically exfoliating HOPG with scotch tape and transferring to highly doped silicon wafer covered with 300 nm SiO₂.²¹ The mono-/bilayer steps are identified by optical contrast and further confirmed by Raman spectrum.²² A typical device is shown in panels b and c in Figure 1. The graphene field-effect transistors (FETs) are fabricated by a previously reported lithography-free method which essentially avoids surface contamination and thermal damage during device fabrication. Briefly, 100 nm thick gold films are

pre-deposited on a silicon wafer. Under an optical microscope, the gold film is tailored into small parts around 20 μm by 100 μm, which are then lifted-off, aligned with graphene and transferred onto graphene by a micromanipulator.²³ By this method, the contact resistance is estimated as 1–2 kΩ (~10 kΩ–μm). Compared with directly depositing metal on graphene, the contact resistance is about 10–15 times larger. However, it is still one order smaller than the channel resistance. In addition, as seen from the output curves and KPFM results, the two terminal resistances present good linearity and the space charge region around the contact is very short. All these results suggest that the contact is “Ohmic-like” (i.e., it is a constant that does not depend on applied source–drain voltage). The electrical measurements are tested by a Keithley 4200 semiconductor analyzer. KPFM are performed on a Bruker Dimension 3100 AFM. To calibrate the contact potential differences (CPD) data from KPFM, the CPD line profile at $V_{ds} = 0$ V is used as a first-order baseline. The CPD line profiles at different biases are then calculated after subtracted from the base line. Generally, the CPD values present a Gaussian distribution. We take the mean as the CPD, and use the 2 RMS as the error bar. All the measurements are carried out under ambient conditions. It worth with mentioning that due to the unintentional substrate doping effect, our devices actually behave as p–p+ junctions under zero gate bias. However, by applying electrical gating, global n type doping can be introduced. For simplicity, the terminology “p–n” junction are used as “p–p+” junction without further notice in the following sections. Depending on surface treatment methods (i.e., thermally depositing organic molecules or mild oxygen plasma), the graphene steps may behave homogeneously or heterogeneously. In the following, we will discuss both cases in detail.

■ RESULTS AND DISCUSSION

Organic Charge Transfer Doping. Firstly, organic charge transfer doping is carried out. Various doping behaviors can be achieved by self-assembling organic charge transfer complex on graphene surface. The interfacial structures of the doped graphene have been substantially studied by photoemission spectroscopy,^{24–26} micro-Raman spectroscopy,^{27–29} scanning tunneling microscopy,³⁰ and KPFM.³¹ The experimental results not only verify this processing technique gives a simple and efficient way to adjust the electronic properties of graphene, but also reveal the thickness-dependent natural of doping strengths. Generally speaking, organic charge transfer doping does not influence the energy dispersion relationships in the momentum space, which keeps graphene as semi-metal on both sides of the interface and leads to a homogenous junction. In this paper, we use self-assembly hexadeca-fluoro-phthalocyaninacopper (F₁₆CuPc) thin film to asymmetrically adjust the electronic properties of graphene flakes: the fluorine atoms remove extra electrons from graphene and result in highly p-type doping effect. This process presents good air robustness and moderate thermal satiability. The doping level can be controlled by the thickness of the self-assembly organic layer as previously reported.^{24,31} It should be mentioned that, in addition to the molecular band-structures and coverage, the molecular orientation also affect the doping effects. Theoretical and experimental works have shown that with a low coverage, the metallophthalocyanine (MPc) molecules trends to adapt a lying down configuration result from the strong π – π interactions.²⁴ In our experiment, 0.5 nm-thick F₁₆CuPc layer is thermally deposited on graphene at a rate of 0.01 Å/s to ensure the smoothness and lying-down configuration. As shown in Figure 2a, the as-prepared graphene FET presents a conventional ambipolar transfer characteristic, suggesting a uniform transport behavior across the whole flake. The Dirac point is measured relative to the back gate voltage as about 20 V. The hysteresis is caused by the trap states, in terms of the substrate dangling

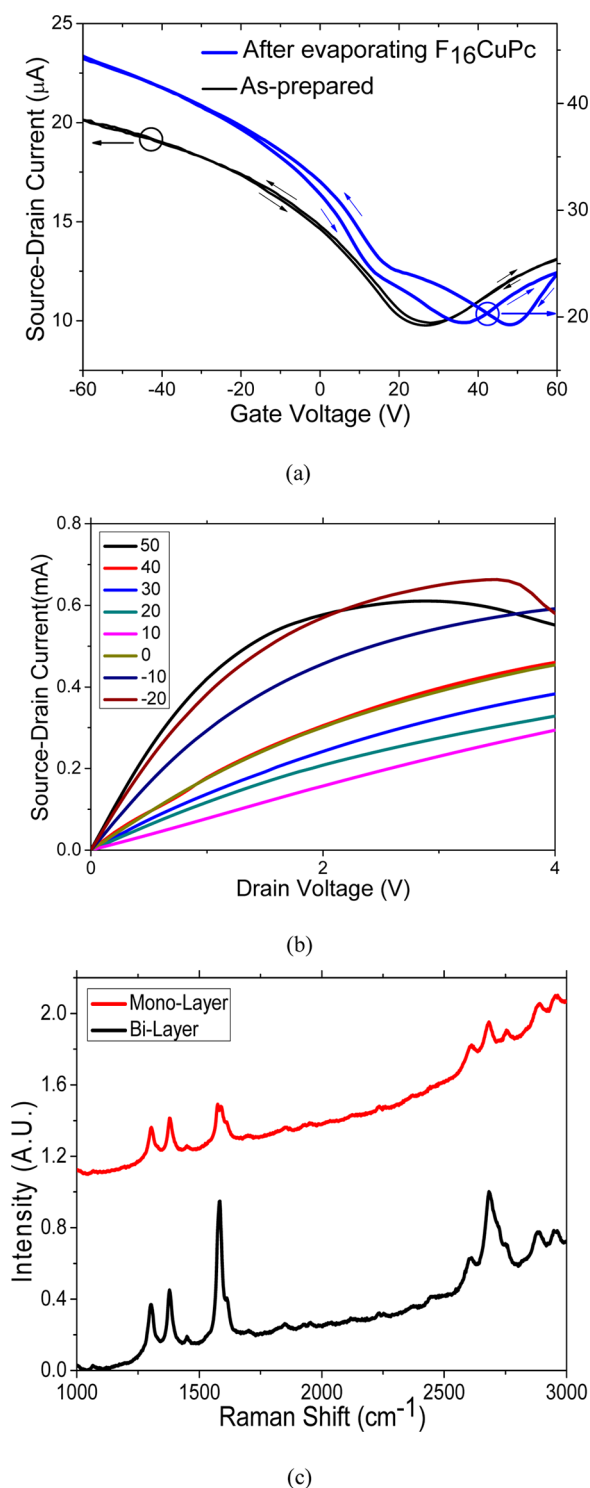


Figure 2. (a) Source–drain current versus applied gate voltage for a graphene step ($W/L = 8 \mu\text{m}/5 \mu\text{m}$). The source-drain voltage is 50 mV. As-prepared (black, left axis) and after evaporating F_{16}CuPc (blue, right axis). (b) Output characteristic of the device in a after evaporating F_{16}CuPc . The bilayer part was grounded as Source. (c) Raman spectra of the device in a after evaporating F_{16}CuPc .

bonds and the surface absorbates. In our experiments, the hysteresis exhibits to a large extent for a single sample, as well as large variations among different samples. We attributed these effects to the relatively high and different values of air humidity during our measurements. However, after facilitating organic

molecules, the molecules present dissimilar doping strength for mono- and bilayer parts due to their different band structures and intrinsic doping of substrate effects (Si–O dangling bond or oxygen absorbates). Figure 2a reveals the field-effect transport after such treatment, which delineates different doping levels and results in a secondary CNP. Generally speaking, the hysteresis increases after surface treatment, indicating the increased trap sites. For organic charge transfer treatment, the trap sites come from the defects in self-assembled layers and molecular dipoles, while for mild oxygen plasma treatment, the defects induced in the graphene basal plane play as the trap sites. To exclude the influence of contact changing, we also tested monolayer control samples and summarized them in the Supporting Information, where the secondary Dirac point is absent. For as-prepared graphene, the mobility and intrinsic hole doping level of as-prepared graphene step are estimated at $3080 \text{ cm}^2/(\text{V s})$ and $2 \times 10^{12} \text{ cm}^{-2}$, respectively. After treatment, the mobility turn to be $4180 \text{ cm}^2/(\text{V s})$ for mono- and $2990 \text{ cm}^2/(\text{V s})$ for bilayer graphene, whereas the hole doping levels are $1.8 \times 10^{12} \text{ cm}^{-2}$ and $2.9 \times 10^{12} \text{ cm}^{-2}$. It worth mentioning that, here, the increased mobility may be an artifact due to the enhanced doping level introduced by the dopant. Nevertheless, the increased conductivity suggests the doping process does not break the π network in graphene basal plane. Interestingly, the current saturation behavior also changes a lot for this graphene p–n junction. NDR is clearly observed for doped steps as illustrated in Figure 2b. We attribute this anomalous output characteristic to the large contrast of carrier sheet density along the channel and the carrier density-dependent saturation velocity. Briefly, because the doping levels and thus the carrier density change dramatically along the channel under high source–drain voltages, the constraint of saturation velocity introduced by the small density part adversely affects the current increase in the whole channel, although the average channel carrier density is large, resulting in a drop of current with an increasing bias voltage. The detailed theoretical modeling and experimental results are discussed elsewhere.^{32,33}

We then move to the doping profiles of our graphene p–n junctions. Raman spectroscopy firstly measures the doping abruptness across the junction.^{34,35} As illustrated in Figure 2c, an obvious peak-shift in Raman spectra is observed for mono- and bilayer region in comparison with as-prepared cases in Figure 1c. However, the most prominent Raman spectral features, i.e., G band around 1580 cm^{-1} and 2D band around 2690 cm^{-1} , are disturbed by the surface treatment in various degrees, which prevent accurately from evaluating the doping attributes via the spectra. For better understanding the junction behavior, surface potential as a function of position along the channel is captured by means of KPFM.^{36,37} Figure 3a shows the contact potential difference (CPD) as a function of position along a typical as-prepared graphene step. From the horizontal profile of these images, we observe a linearly increasing CPD and abrupt kinks at the contacts and junction interfaces. It is worth mentioning that the junction width across the p–n interface is similar to the graphene/metal contact length, suggesting that mono- and bilayer graphene form Ohmic contacts with metals and small lateral screening lengths.

In addition, the homogenous behavior under different source-drain biases reveals the uniform evolution of surface potential distribution across the device. In the whole bias range, the CPDs in bilayer region are about 30 mV higher than those of monolayer parts for the device, whereas the potentials

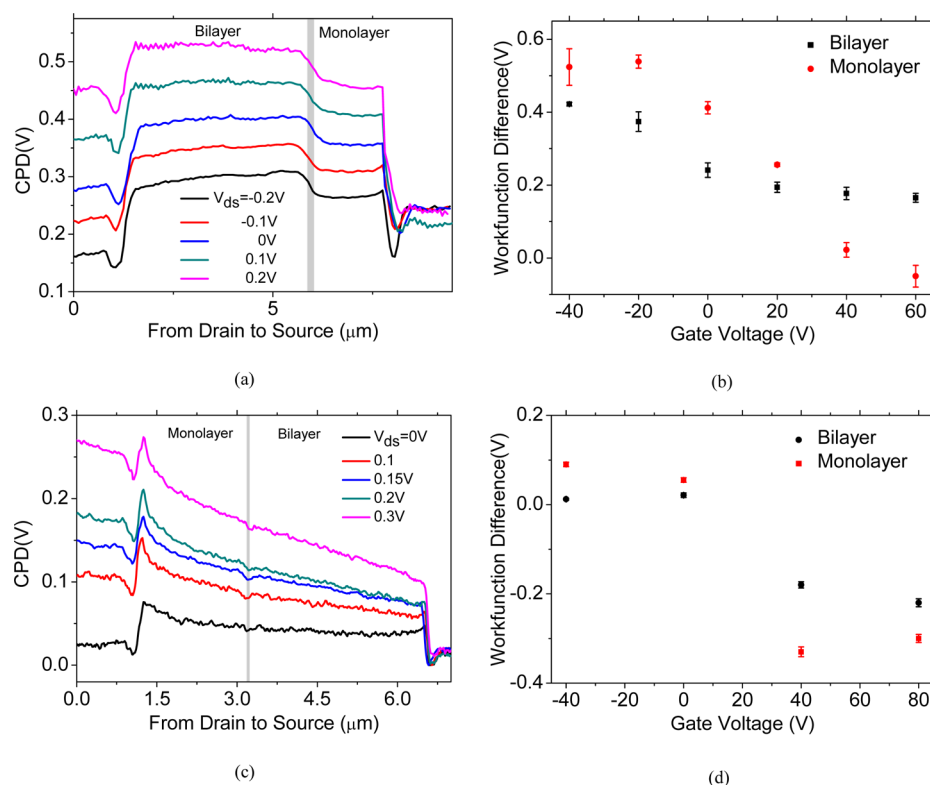


Figure 3. (a) KPFM potentials profile of as-prepared graphene step at zero gate bias. The grey shade indicates the interface between mono- and bilayer graphene. (b) Workfunction difference versus applied gate voltage of the device in a with $V_{ds} = 0$. (c) KPFM potential profile of graphene step after evaporating $F_{16}CuPc$. The grey shade indicates the interface between mono- and bilayer graphene. (d) Workfunction difference versus applied gate voltage of the device in c with $V_{ds} = 0$.

linearly increase along the channel. Figure 3b monitors the surface potential responses to an increasing gate voltage in different parts. The “monolayer-domain” to “bilayer-domain” crossover corresponds to the Dirac point at which the carrier density is the same for both graphene parts. This could be understood by considering the evolution of density-of-states (DOS) with applied gate bias: for hole (electron) doped graphene samples, due to the DOS of bilayer graphene is larger, the Fermi-level is closer to its Dirac point under a similar doping level, creating a lower (higher) surface potential compared with the monolayer case.^{31,38}

After depositing organic molecules, the change in surface potential qualitatively preserves its behavior. As illustrated in Figure 3c, the surface potential also presents homogeneous responses under both source-drain and gate biases, only with modified gate-dependent potential differences. In comparison with the as-prepared step, Figure 3d indicates that the slopes of both parts are almost unchanged, whereas their crossover point is modified because of the unequal charge transfer from molecules to mono- and bilayer parts. Actually, the negative charges transferred from molecules push down graphene’s chemical potential, resulting in a horizontal shift in the V_g –CPD diagram. The different charge transfer of mono- and bilayer parts give rise to different horizontal shifts; as a result, the crossover point is altered.

Mild Oxygen Plasma Irradiation. Covalent surface treatment such as electron-beam or oxygen plasma irradiation is an alternative way to functionalize graphene. Here, we use mild oxygen plasma to treat with graphene steps (5W RF power, Ar/O_2 flow = 0.2/7 SCCM, 3 s). By adjusting the plasma power and exposure time, the doping level could be

continuously controlled. The active oxygen species are covalently attached on the graphene basal plane, partially oxidizing monolayer graphene. Moreover, for bilayer graphene, the top layer protects the underneath one, if the plasma strength is relatively weak, resulting in asymmetric doping effects for mono- and bilayer graphene parts.³⁹ However, in this scenario, the band structures across the step are qualitatively inhomogeneous, in terms of the different changing of linear band structure.

Similar to the surface charge transfer doping, covalent treatment also asymmetrically modifies the Raman spectra and raises a secondary Dirac point in the field-effect transfer characteristics, as shown in panels a and c in Figure 4. The mobility and intrinsic hole doping level of as-prepared graphene step are $3780 \text{ cm}^2/(\text{V s})$ and $1.5 \times 10^{12} \text{ cm}^{-2}$, respectively. After treatment, the mobilities turn to be $1270 \text{ cm}^2/(\text{V s})$ for mono- and $1060 \text{ cm}^2/(\text{V s})$ for bilayer graphene; the doping levels are $1.7 \times 10^{12} \text{ cm}^{-2}$ and $7 \times 10^{11} \text{ cm}^{-2}$. In addition to a decrease of source-drain current, the output curves also distinctly change. A weak rectification effect turns out as illustrated in Figure 4b. This “Schottky-junction-like” curve can be explained by the aforementioned asymmetric modification of graphene band structure, which resulted in a barrier like band bending between mono- and bilayer graphene sheets. However, due to the complicated band properties, i.e., the modified monolayer and bilayer graphene cannot be respectively regarded as ideal semiconductor and metal, the rectification is different from the classical Schottky rectifier. Further works are needed to better understand and optimize the rectifier.

We next use KPFM to study the junction. In the case of covalent functionalization, the measured CPDs non-uniformly

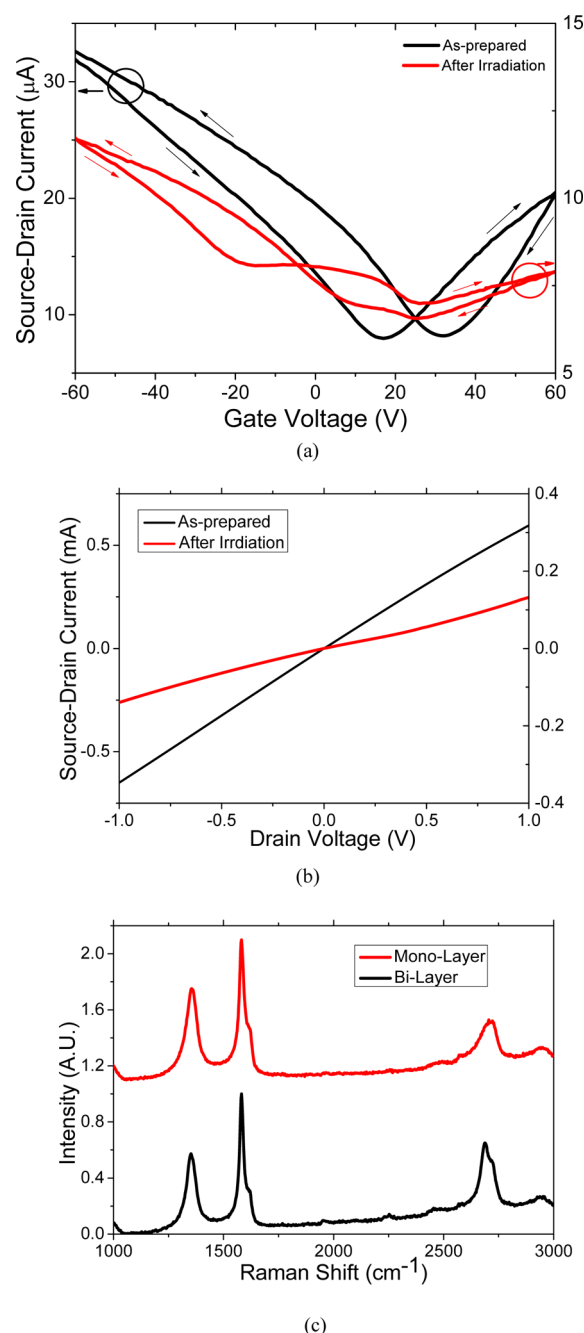


Figure 4. (a) Source–drain current vs applied gate voltage for a graphene step. ($W/L = 10 \mu\text{m}/6 \mu\text{m}$) The source-drain voltage is 50 mV. As-prepared (black, left axis) and after oxygen plasma irradiation (red, right axis). (b) Output characteristic of the device in (a) as-prepared (black, left axis) and after oxygen plasma irradiation (red, right axis) with zero gate voltage. The bilayer part was grounded as source. (c) Raman spectra of the device in (a) after oxygen plasma irradiation.

increase along the channel as summarized in Figure 5a. As the amplitude of the bias increases, the overall CPDs of the monolayer part asymmetrically enlarge while the bilayer ones nearly keep uniform increase. Here again, the contact potential localized between the graphene/metal interface concentrate within a small length, implying that the rectification does not arise from nonideal contact. At the same time, the contact kinks are smeared out after plasma treatment, which implies that some trap states are induced near the contact and block the

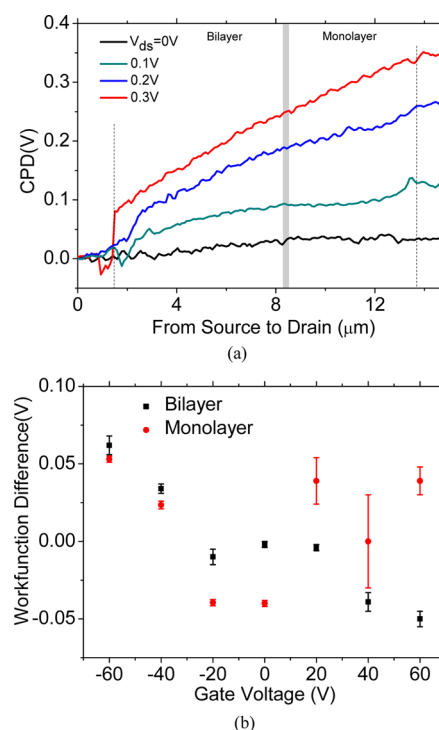


Figure 5. (a) KPFM potential profiles of graphene step after oxygen plasma irradiation at zero gate bias. The grey shade indicates the interface between mono- and bilayer graphene. The dashed lines indicate the electrode edges. (b) Work function difference versus applied gate voltage of the device in (a) with $V_{\text{ds}} = 0$.

sharp work function differences. Remarkably, the potential kink across the interface between mono- and bilayer graphene spreads a long distance relative to the charge transfer doping cases and nonuniformly increases with the lateral bias. At lower bias, the nonuniform part extends to the bilayer side up to a few micrometers, resulting in the rectification effect. In addition, under gate modulation, the monolayer graphene exhibits exotic responses as shown in Figure 5b. It is obvious that after plasma treatment, the electron concentration fluctuates unexpectedly. This anomalous is in accordance with field-effect transport measurements for treated monolayer graphene. As shown in Figure S2 of the Supporting Information, the electron field-effect disappears for treated monolayer graphene. Therefore, the specific band structure of covalently treated monolayer graphene plays a decisive role here. The oxidative sites trap electrons and render gaplike structure. Actually, first-principles calculations and photoluminescence experiments have shown that the oxygen plasma asymmetrically modifies mono- and bilayer graphene, i.e., it partially oxidizes monolayer graphene, but retains zero-gap nature for bilayer part.³⁹ As a result, the graphene step presents a heterostructure feature.

CONCLUSION

In conclusion, we have fabricated two kinds of typical graphene p–n junctions and studied their interfacial properties. We find that through organic surface charge transfer doping, the junction is sharply transformed from p-type (monolayer) region to n-type (bilayer) region. Although the rectification effect is not observed because of the absence of additional resistance in the junction, the output characteristic presents an abnormal NDR behavior. On the other hand, in the case of covalent bond doping, i.e., by oxygen plasma irradiation, the

surface potential transition regions of the junction span up to several hundred nanometers. And the rectification effect is clearly observed in two terminal measurements. We ascribe the distinct behaviors to the band structure variation in different graphene systems: Under organic surface charge transfer doping, because the graphene basal plane is largely reserved, the relatively large carrier density results in a metal-to-metal like junction. However, in the case of the oxygen plasma irradiation, the treatment asymmetrically modifies the linear band structure and therefore a long space charge region is formed, which produces a metal-semiconductor-like junction. Our results not only unveil the detailed properties of graphene p–n junction interface but also gain an insight into its practical applications in nanoelectronics.

■ ASSOCIATED CONTENT

Supporting Information

Transport properties of functionalized monolayer GFET. This material is available free of charge via the Internet at <http://pubs.acs.org>.

■ AUTHOR INFORMATION

Corresponding Author

*E-mail: jbxu@ee.cuhk.edu.hk.

Author Contributions

The manuscript was written through contributions of all authors. All authors have given approval to the final version of the manuscript.

Notes

The authors declare no competing financial interest.

■ ACKNOWLEDGMENTS

The work is in part supported by Research Grants Council of Hong Kong, particularly, via Grants AoE/P-03/08, CUHK4182/09E, CUHK4179/10E, and N_CUHK405/12. J.B.X., J.C. and W.G.X. thank the National Science Foundation of China (Grants 60990314, 60928009, 61229401, 51072236, and 61106093) for support.

■ REFERENCES

- Geim, A. K.; Novoselov, K. S. *Nat. Mater.* **2007**, *6*, 183.
- Huang, X.; Yin, Z.; Wu, S.; Qi, X.; He, Q.; Zhang, Q.; Yan, Q.; Boey, F.; Zhang, H. *Small* **2011**, *7*, 1876.
- He, Q.; Wu, S.; Yin, Z.; Zhang, H. *Chem. Sci.* **2012**, *3*, 1764.
- Abanin, D. A.; Levitov, L. S. *Science* **2007**, *317*, 641.
- Young, A. F.; Kim, P. *Nat. Phys.* **2009**, *5*, 222.
- Zhang, L. M.; Fogler, M. M. *Phys. Rev. Lett.* **2008**, *100*, 116804.
- Cheianov, V. V.; Fal'ko, V.; Altshuler, B. L. *Science* **2007**, *315*, 1252.
- Huard, B.; Sulpizio, J. A.; Stander, N.; Todd, K.; Yang, B.; Goldhaber-Gordon, D. *Phys. Rev. Lett.* **2007**, *98*, 236803.
- Williams, J. R.; DiCarlo, L.; Marcus, C. M. *Science* **2007**, *317*, 638.
- Lohmann, T.; Von Klitzing, K.; Smet, J. H. *Nano Lett.* **2009**, *9*, 1973.
- Cheng, H.-C.; Shiue, R.-J.; Tsai, C.-C.; Wang, W.-H.; Chen, Y.-T. *ACS Nano* **2011**, *5*, 2051.
- Kim, Y. D.; Bae, M.-H.; Seo, J.-T.; Kim, Y. S.; Kim, H.; Lee, J. H.; Ahn, J. R.; Lee, S. W.; Chun, S.-H.; Park, Y. D. *ACS Nano* **2013**, *7*, 5850.
- Farmer, D. B.; Lin, Y.-m.; Afzali-Ardakani, A.; Avouris, P. *Appl. Phys. Lett.* **2009**, *94*, 213106.
- Brenner, K.; Murali, R. *Appl. Phys. Lett.* **2010**, *96*, 063104.
- Baltazar, J.; Sojoudi, H.; Paniagua, S. A.; Kowalik, J.; Marder, S. R.; Tolbert, L. M.; Graham, S.; Henderson, C. L. *J. Phys. Chem. C* **2012**, *116*, 19095.
- Sojoudi, H.; Baltazar, J.; Tolbert, L. M.; Henderson, C. L.; Graham, S. *ACS Appl. Mater. Interfaces* **2012**, *4*, 4781.
- Chiu, H.-Y.; Perebeinos, V.; Lin, Y.-M.; Avouris, P. *Nano Lett.* **2010**, *10*, 4634.
- Yu, T.; Liang, C.-W.; Kim, C.; Yu, B. *Appl. Phys. Lett.* **2011**, *98*, 243105.
- Rao, G.; Freitag, M.; Chiu, H.-Y.; Sundaram, R. S.; Avouris, P. *ACS Nano* **2011**, *5*, 5848.
- Wang, X. M.; Wang, C. L.; Xu, J. *MRS Proc.* **2012**, *1407*, mrsf11.
- Novoselov, K. S.; Geim, A. K.; Morozov, S. V.; Jiang, D.; Zhang, Y.; Dubonos, S. V.; Grigorenko, I.; Firsov, A. A. *Science* **2004**, *306*, 666.
- Ferrari, A. C.; Meyer, J. C.; Scardaci, V.; Casiraghi, C.; Lazzeri, M.; Mauri, F.; Piscanec, S.; Jiang, D.; Novoselov, K. S.; Roth, S.; Geim, A. K. *Phys. Rev. Lett.* **2006**, *97*, 187401.
- Wang, X. M.; Xu, J.-B.; Wang, C. L.; Xie, W. G.; Du, J. *Adv. Mater.* **2011**, *23*, 2464.
- Chen, W.; Chen, S.; Qi, D. C.; Gao, X. Y.; Wee, A. T. S. *J. Am. Chem. Soc.* **2007**, *129*, 10418.
- Coletti, C.; Riedl, C.; Lee, D. S.; Krauss, B.; Patthey, L.; von Klitzing, K.; Smet, J. H.; Starke, U. *Phys. Rev. B* **2010**, *81*, 235401.
- Choudhury, D.; Das, B.; Sarma, D. D.; Rao, C. N. R. *Chem. Phys. Lett.* **2010**, *497*, 66.
- Dong, X.; Fu, D.; Fang, W.; Shi, Y.; Chen, P.; Li, L.-J. *Small* **2009**, *5*, 1422.
- Koehler, F. M.; Jacobsen, A.; Ensslin, K.; Stampfer, C.; Stark, W. J. *Small* **2010**, *6*, 1125.
- Das, B.; Voggu, R.; Rout, C. S.; Rao, C. N. R. *Chem. Commun.* **2008**, 5155.
- Wang, Q. H.; Hersam, M. C. *Nat. Chem.* **2009**, *1*, 206.
- Wang, X. M.; Xu, J.-B.; Xie, W. G.; Du, J. *J. Phys. Chem. C* **2011**, *115*, 7596.
- Wang, X. M.; Xu, H.; Min, J.; Peng, L.-M.; Xu, J.-B. *Nanoscale* **2013**, *5*, 2811.
- Wu, Y.; Farmer, D. B.; Zhu, W.; Han, S.-J.; Dimitrakopoulos, C. D.; Bol, A. A.; Avouris, P.; Lin, Y.-M. *ACS Nano* **2012**, *3*, 2610.
- Casiraghi, C.; Pisana, S.; Novoselov, K. S.; Geim, A. K.; Ferrari, A. C. *Appl. Phys. Lett.* **2007**, *91*, 233108.
- Das, A.; Pisana, S.; Chakraborty, B.; Piscanec, S.; Saha, S. K.; Waghmare, U. V.; Novoselov, K. S.; Krishnamurthy, H. R.; Geim, A. K.; Ferrari, A. C.; Sood, A. K. *Nat. Nanotechnol.* **2008**, *3*, 210.
- Yu, Y.-J.; Zhao, Y.; Ryu, S.; Brus, L. E.; Kim, K. S.; Kim, P. *Nano Lett.* **2009**, *9*, 3430.
- Wang, X.; Xie, W.; Du, J.; Wang, C.; Zhao, N.; Xu, J.-B. *Adv. Mater.* **2012**, *24*, 2614.
- Ziegler, D.; Gava, P.; Güttinger, J.; Molitor, F.; Wirtz, L.; Lazzeri, M.; Saitta, A. M.; Stemmer, A.; Mauri, F.; Stampfer, C. *Phys. Rev. B* **2011**, *83*, 235434.
- Nourbakhsh, A.; Cantoro, M.; Klekachev, A. V.; Pourtois, G.; Vosch, T.; Hofkens, J.; van der Veen, M. H.; Heyns, M. M.; De Gendt, S.; Sels, B. F. J. *J. Phys. Chem. C* **2011**, *115*, 16619.